Effects of Low-Frequency Wave Interactions on Intraseasonal Oscillations

Paul E. Roundy

NOAA–CIRES Aeronomy Laboratory, Boulder, Colorado

William M. Frank

Department of Meteorology, The Pennsylvania State University, University Park, Pennsylvania

(Manuscript received 13 February 2004, in final form 14 June 2004)

ABSTRACT

Intraseasonal oscillations (ISOs) control much of the large-scale variability of convection in the Tropics on time scales of about 15–100 days. These disturbances are often thought to be dominated by eastward-propagating modes, especially during austral summer, but disturbances that propagate westward are also important.

This work demonstrates by means of a multiple linear regression model and a brief case study that eastward- and westward-moving intraseasonal modes often cooperatively interact with one another to produce many of the characteristics of the observed Southern Hemisphere summer ISO. These interactions appear to be facilitated by topography and/or by the convective anomalies that are cooperatively induced by the eastward- and the westward-moving components of the oscillations. These interactions do not occur during every period of intraseasonal convective activity, but they do commonly occur during periods of high-amplitude convective anomalies. This analysis shows that eastward- and westward-moving intraseasonal modes should not be generally assumed to be linearly independent entities.

1. Introduction

a. Linear and nonlinear interactions

Intraseasonal oscillations (ISOs), including the Southern Hemisphere summer Madden–Julian oscillation (MJO; Madden and Julian 1994), are 20–60-day fluctuations of tropical winds and convection that are largely characterized by zonal wavenumbers 1–4. Studies of these low-frequency variations have improved our understanding of the tropical atmosphere and may enhance intraseasonal weather predictability. Since the discovery of the MJO in 1971, much attention has been focused on eastward-propagating modes in isolation from westward-propagating modes. One view of the MJO is that interactions between eastward- and westward-propagating modes may not be important on large scales and that eastward propagation dominates the process (e.g., Zhang and Hendon 1997, hereafter ZH97). The Northern Hemisphere summer ISO (NHISO) is thought to be more complicated because westward and meridionally propagating modes appear to play a more significant role (Kemball-Cook and Wang 2001).

In this study, we show that ISOs exhibit significant standing and sometimes even westward-propagating behavior, regardless of the season. We also find that large-scale westward-propagating modes play key roles in ISOs, even during seasons when eastward propagation appears to dominate. These westward-moving modes include the meridional mode $n = 1$ equatorial Rossby wave described by Wheeler and Kiladis (1999, hereafter WK99), Roundy and Frank (2004a), and many others. They also include possible higher-mode Rossby waves (Matsuno 1966) and patterns that are asymmetric with respect to the equator. We argue that ignoring the westward-propagating components of these processes limits our abilities to understand intraseasonal behavior and its origins. Including westward propagation in studies of these processes reveals origins of and sources of amplification of eastward-propagating anomalies and should enhance our ability to forecast intraseasonal convection and rainfall in the Tropics. To simplify the discussion, we label the eastward-propagating portion of the ISO the ISOe and the westward-propagating portion the ISOw.

Interactions between the ISOe and the ISOw is a relatively new subject. Yanai et al. (2000) and others discuss how the MJO and atmospheric waves may interact to modify the distribution and variability of convection, but they do not address nonlinear interactions by which one wave may modify the structure of another wave. Kemball-Cook and Wang (2001) and Wang and Xie (1997) address some interaction of NHISO eastward-

---

Corresponding author address: Paul Roundy, NOAA–CIRES Aeronomy Laboratory, R/AL3, 325 Broadway, Boulder, CO 80303-3328.
E-mail: proundy@al.noaa.gov

and westward-propagating modes. They discuss a process that we claim is similar at least in some respects to wave reflection, by which westward-moving disturbances help excite new ISOe events near East Africa. In this process, westward-moving off-equatorial convective anomalies associated with equatorial Rossby (ER) waves arrive near East Africa where they appear to excite eastward-moving anomalies near the equator. We speculate that this excitation may be facilitated by dynamical Rossby wave (partial) reflection from the East African Highlands or by enhancement of equatorial convection by the Rossby wave as it interacts with both land and sea near the African coast. The dynamics of such apparent reflections are difficult to determine by observations alone. We therefore term the process reflection, though we do not show that it is dominated by the dynamical reflection of a wave from a barrier.

There is theoretical motivation for studying nonlinear behavior on the scales of the ISO. Linear models, like those of Matsuno (1966), may begin to break down when applied to the atmosphere in this portion of the spectrum, because these models ignore the nonlinear advection terms and convective feedbacks. The advection terms may be ignored only if the background winds through which a wave propagates are much smaller than the phase speeds of the waves. A simple scale analysis applied to the $n = 1$ ER wave in the presence of the MJO and no other background flow reveals that the MJO winds are sufficient to distort the structure and propagation statistics of the ER waves. In this scale analysis, the effects of advection of the ER waves by anomalous winds of the ISOe are of the same order of magnitude as the partial derivative with respect to time of the winds induced by an ER wave in the absence of background flow. In addition to the nonlinearity contributed by this dynamical interaction, any interactions between the waves associated with feedbacks from cooperatively excited convection may also contribute an important nonlinear component.

b. *Standing oscillations of the ISO*

The simplest interaction that we observe between eastward- and westward-propagating anomalies results in the production of standing behavior. This type of interaction may be mostly linear, meaning that waves propagating in the same environment may not need to modify each other to generate the observed behavior. Discussion of the standing behavior associated with intraseasonal convection is not new. Many modeling studies assume that the MJO is maintained by a fluctuating heat source (e.g., Yamagata and Hayashi 1984; Anderson and Stevens 1987; Chang 1977; Hayashi and Miyahara 1987; Itoh and Nishi 1990; Hu and Randall 1994) that could be a quasi-standing oscillation in convection.

Yanai et al. (2000) noted standing variations in convection over equatorial Africa, the Maritime Continent region, and South America. Pairs of standing anomalies occasionally form seesaws in convection in several regions (Lau and Chan 1986; Zhu and Wang 1993), meaning, for example, that one anomaly over the west Pacific is often paired with another anomaly with an opposite sign over the Indian Ocean. The anomalies within the pair alternate sign. Longitude–time diagrams of both modeled and satellite-measured outgoing longwave radiation (OLR; e.g., ZH97; Hu and Randall 1994), precipitable water (PW; shown below), and wind (e.g., Lin et al. 2000) data also seem to reveal that apparent standing oscillations on the time scale of the ISO occur in many regions.

ZH97 performed a variety of statistical analyses of global tropical OLR to investigate possible standing oscillations. They concluded that no dominant standing component of the ISO could be identified in observations and that what appears as a standing oscillation is actually caused by base-state modulation of the amplitude of eastward-moving anomalies. Their analysis assumes that standing behavior confined to specific regions and seasons would be significant in a global analysis.

ZH97 did not address that the ISOw is dominated by waves projecting onto ER modes (WK99; Kiladis and Wheeler 1995; Roundy and Frank 2004a). These ER waves may comprise much of the westward-propagating component of intraseasonal standing behavior. We propose that intersection of ER waves with the MJO can cause regional enhancement or suppression of convection along the path of the MJO, resulting in standing behavior when these intersections tend to occur at preferred locations. ZH97 did not directly address the effects of interactions between ER waves and the MJO upon the overall pattern of OLR fluctuations in the 15–100-day period range. Such interactions are a major focus of the current paper.

c. *Interactions between the ISOe and equatorial Rossby waves*

Wang (1988), Madden and Julian (1994), Lindzen (1974), Chang (1977), and others have stated that, in spite of some important differences, the structures of observed ISOe disturbances are similar to those of long equatorial moist Kelvin waves. The strongest argument for applying this rough approximation to most ISOe disturbances is that they are dominated by alternating anomalous zonal winds that tend to have the highest amplitude near the equator. Under this assumption, the westward-propagating part of the spectral decomposition of any ISOe-related quasi-standing activity must consist of waves that are structurally and dynamically different from the Kelvin-wave-like core of the ISOe, because theory precludes a westward-propagating mode that resembles a Kelvin wave.

If the ISOe behaves to a first approximation like a long equatorial Kelvin wave, then one may examine existing theory that associates Kelvin waves with ER waves to gain some insight into the problem. Existing theory explains how ER waves and Kelvin waves may excite one another both through interactions with topography and through the release of latent heat in deep convection. A Kelvin wave may partially reflect from an eastern topographical barrier to form a group of westward-propagating ER waves (e.g., McPhaden and Gill 1987). Further, a group of ER waves may reflect from western barriers to form a Kelvin wave (Kleeman 1989).

Equatorial Rossby waves may also be generated by convection within ISOe events. Frictional wave conditional instability of the second kind (CISK) theory (Salby et al. 1994) associates Rossby-like models with an eastward-propagating mode similar in some ways to the MJO. The ER waves propagate westward away from the large-scale organized convection that excites them.

Observations confirm many of these relationships between similar eastward- and westward-propagating waves in both the ocean and the atmosphere. Battisti (1988), Kang and An (1998), and others discuss quasi-standing oscillations in sea surface temperature (SST) associated with the interaction of oceanic Kelvin and ER waves. The standing behavior occurs near wave reflection points. Figure 1 of Park and Schubert (1993) indicates similar quasi-standing waves in the atmosphere near the Andes Mountains of South America. They found that these oscillations are associated with the MJO as it moves into the region from the Pacific basin. Hendon and Salby (1994) and Kemball-Cook and Wang (2001) observed ER waves that appeared to be generated by eastward-propagating intraseasonal convective events.

This study explores the manner in which the ISOe and ER waves cooperate to produce specific patterns of enhancement or suppression of moist deep convection and how the ISOe and the ISOw cooperate to modify and sustain each other. This work examines whether such interactions cause many of the standing oscillations in convection that are frequently observed in the ISO frequency band. Further, this paper explores whether ER waves trigger new ISOe disturbances and/or amplify existing ones near East Africa and whether the ISOe also excites new ER waves near the west coast of the Americas. The results reveal a systematic process by which eastward- and westward-propagating modes sustain one another during periods of strong intraseasonal convective activity. These interactions are the cause of many attributes of the intraseasonal oscillations, and are therefore a fundamental and important part of global weather and climate.

2. Data and methods

a. Data

We apply filtering and lagged regression approaches to OLR, PW, and wind data to separate and composite the eastward- and westward-propagating waves that are associated with the low-wavenumber portion of the ISOe. Interpolated OLR data [from the National Oceanic and Atmospheric Administration (NOAA) near-polar-orbiting satellites] were acquired from the Climate Diagnostics Center (CDC) on a 2.5° grid (Liebmann and Smith 1996). The NASA Water Vapor Project (NVAP) provided daily PW data on a 1° grid (Randel et al. 1996). The PW data are useful in this analysis because PW anomalies trace disturbances through regions where large-scale organized convection is suppressed by the base state. The difference between PW variance in convective and nonconvective regions is not as great as the difference between the OLR variances in the same regions. Here PW and OLR anomalies closely track one another in regions where deep convection is active, except that PW anomalies tend to lead OLR anomalies slightly. The main advantage of the PW anomalies is that, when OLR anomalies become insignificant through the Western Hemisphere, the PW continues to show significant patterns. These Western Hemisphere PW anomalies appear to be enhanced by the effects of meridional vapor advection by the waves across the narrow intertropical convergence zones. The main disadvantage of the PW data is that they are only available for a 10-yr period. We also studied about 30 yr of OLR data and found patterns similar to those discussed below, except that the anomalies seen in the Western Hemisphere have less significant amplitudes then are shown in the PW anomalies.

Daily pressure level wind data on a 2.5° grid were obtained from the National Centers for Environmental Prediction–National Center for Atmospheric Research (NCEP–NCAR) reanalysis project. These wind data were used in horizontal maps of the composite data. All data were limited to the period 1 January 1988 through 31 December 1997 because that is the range of availability of the PW data.

The daily global OLR, PW, and wind data from 20°S to 20°N were processed as discussed in Roundy and Frank (2004a). Processing included removing the annual cycle before applying filtering in the wavenumber–frequency domain.

b. Filtering

We designed two Fourier filters to isolate the space–time behavior associated with specific regions of the zonal wavenumber–frequency space of these anomalies (WK99; Roundy and Frank 2004a). The filters were labeled ISOe and ISOw. The ISOe filter contains the region generally accepted to describe the MJO, including wavenumbers 0–6 eastward and periods of 26–104 days. The ISOw filter includes westward propagation, wavenumbers 1–6, and periods of 15–104 days. The ISOe band does not extend into the 15–25-day period range in order to avoid contamination from the convectively coupled Kelvin wave mode that occurs in that region that may not be directly related to the MJO (e.g., WK99; Straub and Kiladis 2002). The ISOw filter overlaps with most of the $n = 1$ ER filter of WK99. Our use of the ISOw filter instead of the $n = 1$ ER filter of WK99 is motivated statistics and by the relevance of specific portions of the spectrum to this analysis. Figure 6b of WK99 indicates that the lower-frequency portion of the dominant peak in the ISOw range lies outside of their $n = 1$ ER band. Our ISOw filter encloses more of the low-frequency portions of the peak, which may be relevant to the ISO. The amount of significant power in this region may have been underestimated by WK99 because their significance test depends on assumptions about the nature of the true background noise spectrum. The background spectrum applied by WK99 overestimates the true noise spectrum because their method of smoothing the total spectrum to obtain a background conserves and redistributes power generated by the waves themselves. This uncertainty about the background spectrum indicates that even further expansion of the ISOw filter to lower frequencies cannot be ruled out by the normalized spectrum of WK99. Such further expansion is required in order for the filter to include the westward-propagating portion of any potential standing component of the ISOs. Further expansion of the filter also allows it to include the signals of higher-mode ER waves, which occur at lower frequencies than the first mode (see below). The relationships discussed below are visible in these filtered datasets, but compositing as discussed below clarifies the relationships because many westward-moving intraseasonal anomalies are not linked with the ISOe.

c. Lagged regression compositing

1) REGRESSION TECHNIQUE

After filtering, we applied two sets of lagged multiple linear regression analyses. These two analyses composited the parts of the eastward-propagating waves and the parts of the westward-propagating waves that are associated with and statistically determined by the largest-scale eastward-propagating OLR anomalies of the ISOe dataset. Applying the directional filtering before compositing guarantees that the composited data will show the imposed direction of propagation, but it does not impose any level of statistical significance or structure on the result.

Multiple linear regression is useful for determining the statistical relationship between sets of correlated variables. Wilks (1995) and von Storch and Zwiers (1999) discuss the general details of the method. Our lagged regression models find and express a statistical relationship between a predictand time series $y(t)$ and a predictor time series $x(t)$ at a time lag τ and the grid point s as in Eq. (1):

$$y_{s,t+\tau} = a_{0,s,\tau} + a_{1,s,\tau}x_t^1 + a_{2,s,\tau}x_t^2 + a_{3,s,\tau}x_t^3 + a_{4,s,\tau}x_t^4 + \varepsilon_{s,\tau}, \tag{1}$$

where y is the modeled variable (ISOw and ISOe band-filtered PW) and x is the predictor variable (ISOe band OLR at a base point, as discussed below). The term ε represents the model residuals. The a_n coefficients are regression parameters that are determined by a simple matrix operation. Roundy and Frank (2004b) discuss the model itself more completely. They show the contributions of the nonlinear terms and demonstrate that they do model nonlinear interactions by which the ISOe modulates the amplitude and frequency of the ISOw (see also Wilks 1995; Draper and Smith 1966).

2) COMPOSITING TECHNIQUE

Composites were generated by utilizing regression equations for the ISOe and ISOw band PW and wind data at each grid point and for a range of time lags. This was done by setting y equal to ISOw or ISOe filtered data and by setting x equal to a time series of filtered OLR at a base point.

The base point was chosen to be 10°S, 90°E [near the point of maximum equatorial OLR variance attributable to the MJO as discussed by WK99 and by Roundy and Frank (2004a)]. The base-point time series was taken from OLR data filtered for periods of 26–104 days and eastward wavenumbers 1–4. This narrow wavenumber band ensures that the regression model results for the broader portions of the spectrum are statistically determined by the region of the spectrum generally accepted to describe the MJO. Only those time periods in which a 60-day windowed variance of the base-point time series exceeded the variance of the entire base point series were included in the calculations. This ensures that results are determined by data from time periods when the signal was present at the base point (e.g., Hendon and Salby 1994; Wheeler et al. 2000).

The location of the base point at 10°S emphasizes the southern summer in the analyses because most of the ISOe band variance there occurs during the southern summer and because periods with relatively low variance were eliminated from the regression. We tested other base points north and south of the equator to emphasize different seasons and to distinguish between the southern summer MJO and the NHISO. We found that the interaction and reflection behavior occurs throughout the year, but with varying statistics. Behavior that may be consistent with eastward deflection of westward-moving convective anomalies near East Africa has already been noted by Kemball-Cook and Wang (2001), but only during the northern summer, so we decided to attempt to find the behavior in data dominated by the southern summer, when the ISOe has the highest amplitude and the strongest global signal (Roundy and Frank 2004a). The strong southern summer signal has the distinct advantage of being more homogeneous than the northern summer signal, or the signal averaged over the entire year. The northern and southern summer ISOs differ in dominant frequencies and anomaly spatial scales (e.g., Wang and Xie 1997). These differences make the amplitudes of composite ISOs that include the entire year insignificant beyond one cycle (e.g., Hendon and Salby 1994). The homogeneity during the southern summer allows our southern-summer-dominated composite to exhibit a greater number of significant cycles than composites that include data for the entire year. This enhancement allows more effective study of interactions that can occur on time scales longer than one ISOe cycle.

3) STATISTICAL SIGNIFICANCE

Statistical significance of the results of this compositing technique was determined by using the bootstrap method (Wilks 1995). These tests and their results are described in appendix A.

3. Results

a. Longitude–time lag composite

Figures 1–4 show the composite results. Figure 1 represents the time lag–longitude evolution of the ISOe and ISOw composite PW in a way that clarifies relationships between the ISOe and the ISOw. These results are developed from many events and thus reveal patterns that occur on average in the set of high-amplitude events in the data.

Figure 1a represents the lag–longitude evolution of the ISOe PW composite at the equator. Figure 1b shows the lag–longitude evolution of the ISOw PW composite, averaged from 2.5° to 7.5°N. These different latitude bands were selected because the ISOw-filtered PW varies most a few degrees off the equator, whereas ISOe-filtered PW varies more near the equator. This distinction is also motivated by theoretical arguments, because eastward-moving Kelvin-like waves produce the most variance of convection on or near the equator, whereas ER waves generate the most variance off the equator. Additionally, when ISOe anomalies are averaged between the equator and 7.5°N, the amplitude is strongly reduced in some regions because ISOe anomalies occasionally switch sign along a longitude line. Our averaging allows the eastward- and westward-propagating anomalies to be traced around the globe. Any distortion caused by this averaging is clarified by plan view maps shown later in Figs. 2 and 3.

To facilitate interpretation, curves that approximately represent the trajectories of propagation are subjectively drawn on the anomalies in Figs. 1a and 1b. In Fig. 1a, solid lines indicate positive anomalies and dashed lines indicate negative anomalies. Heavy dashed lines in Fig. 1b indicate positive anomalies and dotted lines trace negative anomalies. It is important to note that Fig. 1a is almost identical to a composite developed from the linear term alone (not shown), revealing that the nonlinear terms contribute little to the ISOe model in comparison to what these terms contribute to the ISOw model. The trajectories in Figs. 1a and 1b are overlaid in Fig. 1c exactly as they appear in 1a and 1b. The evolution of the ISOe/ISOw system may be traced over cycles in Fig. 1c.

In Fig. 1a, ISOe anomalies propagate slowly eastward ($\sim$5 m s^{-1}) over the Indian and western Pacific Oceans, then accelerate eastward across the remainder of the Pacific and through the Western Hemisphere (up to 20 m s^{-1}). Hendon and Salby (1994), Yanai et al. (2000), and others have shown similar patterns of acceleration across the Western Hemisphere. The dominant period of the composite ISOe is about 50 days. A temporary decrease in anomaly amplitude occurs between the Indian and west Pacific Ocean basins (consistent with the results of ZH97 and others), followed by a more significant decrease in amplitude through the Western Hemisphere.

Many of the displayed ISOw anomalies in Fig. 1b are continuous from the Andes Mountains to East Africa, although their amplitudes and phase speeds change with longitude and lag. These waves are probably not generated directly by ISOe-induced convection because they tend to form in a region of the east Pacific where ISOe-related convection is weak. Nevertheless, because the composites are calculated relative to an ISOe index, we know that these waves are associated with the ISOe.

Comparison of Figs. 1a and 1b reveals evidence of nonlinear interactions between the eastward- and the westward-propagating PW anomalies. The PW anomalies associated with the westward-propagating waves amplify as they propagate through the active (high PW) phases of the ISOe. This amplification gives the illusion that the higher-amplitude waves form progressively eastward, resulting in an eastward pseudogroup velocity associated with the higher-amplitude westward-propagating waves. For example, relative extrema of succeeding amplified ISOw PW anomalies occur along the thin lines labeled GV1 and GV2. These lines demonstrate that the successive anomalies that they trace peak progressively farther east. If the ISOw is indeed dominated by equatorially trapped long ER waves, then this is inconsistent with shallow-water theory, which predicts that these ER waves that are characterized by wavenumbers less than 10 should have a westward group velocity (Matsuno 1966; WK99). Figure 1a reveals another possible explanation for the behavior in Fig. 1b. The lines GV1 and GV2 nearly coincide with ISOe trajectories labeled (2) and (3) in Fig. 1a. A minimum in ISOw anomaly amplitudes occurs along the trajectories between the lines GV1 and GV2. That minimum is collocated with ISOe trajectory (1) in Fig. 1a, where PW is low and convection is suppressed. This shows that ISOw anomaly amplitudes tend to be reduced in regions where ISOe PW anomalies are negative. In addition to the pseudogroup velocities, additional westward-propagating anomalies occur along the lines GV1 and GV2 that are not continuous between the Andes

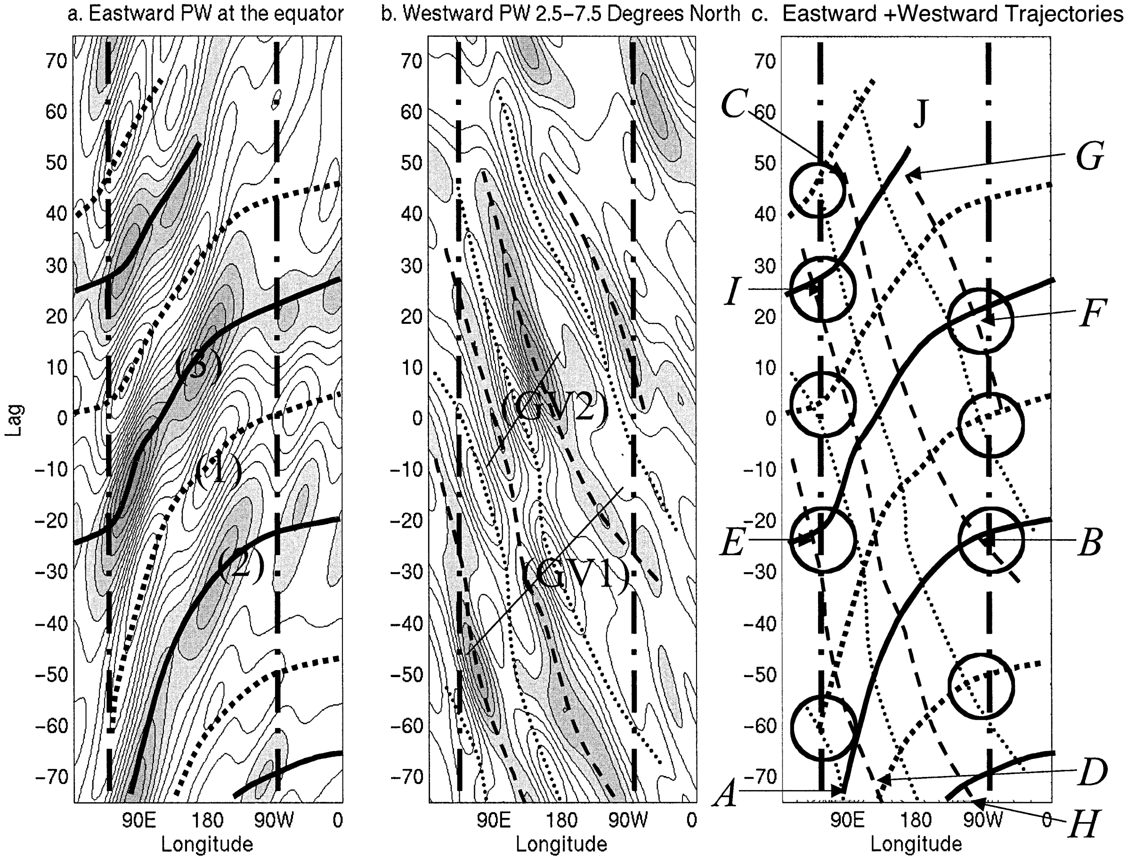

FIG. 1. (a) Longitude–time lag representation of the composite eastward-propagating part (ISOe) of the precipitable water anomaly, determined by filtered OLR at 10°S, 90°E. The time lag represents the time before and after an OLR anomaly two standard deviations below the mean crosses 90°E at the equator. (b) As in (a) except for the westward-propagating part of the precipitable water anomaly determined by the same OLR series as in (a). (c) The trajectories of (a) + (b). Curves drawn in (a)–(c) represent approximate trajectories of anomaly propagation. Locations labeled *A–J* are discussed in the text. Circled locations in (c) represent intersection points of eastward- and westward-propagating modes of the same sign that occur near the Andes Mountains and the East African Highlands. The contour interval in (a) and (b) is 0.5 mm, centered on zero.

Mountains and Africa, indicating that the frequency and wavenumber of the westward-propagating waves both increase as the westward-propagating waves pass through the active ISOe regions and amplify. Roundy and Frank (2004b) give further discussion about the contribution of the nonlinear terms to the composite view of these interactions.

Effects of advection on the ISOw seem to be apparent in Fig. 1b. A temporary increase in trajectory slopes occurs between the lines GV1 and GV2, representing slower phase propagation there. Composited 300-hPa winds (not shown) reveal a shift from easterly to westerly at the same location, indicating that trajectory (1) is just west of a line of upper-level convergence (consistent with the lower PW values there). Doppler shifting of ISOw waves in the region of the strongest anomalous westerlies immediately west of (1) may slow the westward progression of the ISOw PW anomalies until they move west of the region. The apparent accelerations appear to be consistent with the effects of advection, because the fastest westward propagation occurs when the background flow is easterly. The winds at many altitudes may cause Doppler-shifting effects on these deep tropospheric waves, and it is not known which altitude is most important. Active convective coupling is also known to slow wave propagation (e.g., WK99).

The mean phase speed of the westward-propagating waves in Fig. 1b is between 3.25 and 4.5 m s^{-1}, or between one-third and one-half the magnitude of the global-mean phase speed of the composite ISOe. These composite waves travel from the east Pacific to the western Indian Ocean basins in about the same time that it takes an ISOe event to circumnavigate the globe two-and-one-third times. However, we find that this relationship varies seasonally. For example, a composite that was calculated from data dominated by the northern summer (not shown) has an ISOe event that circumnavigates the globe one-and-one-third times in the time that it takes the associated ISOw anomalies to cross from the east Pacific basin to the western Indian Ocean. This seasonal variability in the westward-moving waves causes westward propagation to be largely absent from

ISOe-based composites that include the entire year (e.g., Hendon and Salby 1994) because the differing seasonal signals largely average each other out. Further analysis (discussed below) indicates that the faster westward-moving wave that occurs during the northern spring and summer is dominated by the first meridional Rossby mode, whereas the slow wave that occurs during the northern winter is dominated by the second mode.

Behavior consistent with wave reflections in the composite relationship between the ISOe and the ISOw can be seen in Fig. 1c. The curves overlaid from Figs. 1a and 1b intersect approximately where extrema of eastward and westward propagating anomalies directly interact. Several interaction points near the East African Highlands and the Andes Mountains are marked with circles. Selections of these are labeled *B*, *E*, *F*, and *I*. Points *B* and *F* are located near the Andes Mountains. Points *E* and *I* are located near East Africa. The alignment near the mountains is not coincidental and is qualitatively consistent with theoretical Kelvin and ER wave reflection (Fig. 9 of McPhaden and Gill 1987; Kleeman 1989). The locations of these points are little affected by the inclusion of the nonlinear terms in the model. The linear term dominates the apparent reflection behavior because the reflected waves have the same frequency as the ISOe close to the reflection points. For the purpose of discussion, we label propagation trajectories from one point to another by combining pairs of point labels (e.g., *B* to *C* as ‘‘*BC*’’).

We discuss two apparent reflections from the Andes and another two from East Africa. Figure 1 reveals several other examples of such events. As the first example, an eastward-propagating anomaly follows the trajectory *AB*. At *B*, it interacts with the mountains. A westward-propagating PW anomaly then amplifies at *B* and follows the trajectory *BC*. As the second example, an ISOw PW anomaly propagates westward from *D* and apparently reflects from East Africa at *E*. The resulting ISOe anomaly propagates eastward across the Indian and Pacific Oceans to the Andes Mountains (at *F*), where another reflection occurs, resulting in a new westward-propagating anomaly that we trace to *G*. Another apparent reflection from Africa occurs at point *I*, where ISOw trajectory *HI* appears to reflect and then enhance ISOe trajectory *IJ*.

These interactions are not limited to one ISOe or ISOw anomaly apparently reflecting to produce another anomaly propagating in the opposite direction. In this regression model, whenever an ISOw anomaly appears to reflect from East Africa, it does so at about the same time that the previous ISOe anomaly arrives there from the Western Hemisphere. This indicates that new high-amplitude ISOe disturbances in the Indian Ocean basin may often be excited by cooperative interaction between apparent reflection of ISOw disturbances (as in Kemball-Cook and Wang 2001) and the arrival of an existing ISOe disturbance from the west (e.g., Yanai et al. 2000). This may be described as a type of resonant response that helps to amplify specific waves with the time scale of the MJO over the western Indian Ocean. In spite of the differences between the ISOe and Kelvin waves, the phase speed of the composite ISOe is often about double that seen in the composite ISOw immediately after reflection, consistent with the theoretical result for Kelvin wave reflection shown in Fig. 9 of McPhaden and Gill (1987). Whether or not the process that occurs near East Africa is a true dynamical wave reflection, these regression model results imply that strong ISOe convective events tend to form after eastward- and westward-moving waves come in phase with one another near East Africa.

The longitude–time lag diagrams (Fig. 1) of the composite are further enhanced by the composite horizontal structures of the ISO band waves that are shown in Figs. 2 and 3. These maps provide information about the horizontal structures of the disturbances traced in Fig. 1.

b. Composite ISOw plan view

ISOw band-filtered PW and wind anomalies in Fig. 2 reveal a pattern of distorted ER modes of a variety of time and space scales. These waves must be modified from their theoretical forms by the base state, background winds, by interaction with land, and by feedbacks from moist convection. Some of the numerous westward-propagating gyres visible in Fig. 2 are labeled with the letter G. It is useful to interpret these distorted waves in the context of theoretical wave structures. Matsuno (1966) shows the horizontal wave structures. The first-mode Rossby wave consists of gyres arranged in pairs across the equator that respond to a pressure field that is symmetric across the equator. Mode-2 waves have gyres rotating in one direction centered on the equator that are flanked on the north and south by larger gyres rotating in the opposite direction, reflecting an antisymmetric pressure field. Numerous sets of gyres in Fig. 2 appear to reflect the distorted structures of both of these modes.

The wave responsible for the trajectory labeled *HI* in Fig. 1c is visible at a lag of −30 days in Fig. 2a, where its PW anomaly is labeled *HI*. This disturbance is characterized by a clockwise gyre located near the equator around 140°E, flanked on the north and south by counterclockwise gyres. This structure is similar to that of an $n = 2$ Rossby wave. The *HI* anomaly propagates westward in subsequent images and dissipates over East Africa. Simultaneous with the arrival of *HI* over East Africa, an eastward-moving anomaly (labeled *IJ*) amplifies in the same region (see Figs. 1a and 3f–h) consistent with the reflection process discussed above.

The most prominent ISOe event shown in Fig. 1 (trajectory *EF*) began when the anomaly-following trajectory *AB* arrived from the west and trajectory *DE* arrived from the east. Anomaly *DE* (shown in Figs. 2a–c) is associated with a wind anomaly that suggests some antisymmetry consistent with the mode-2 Rossby wave

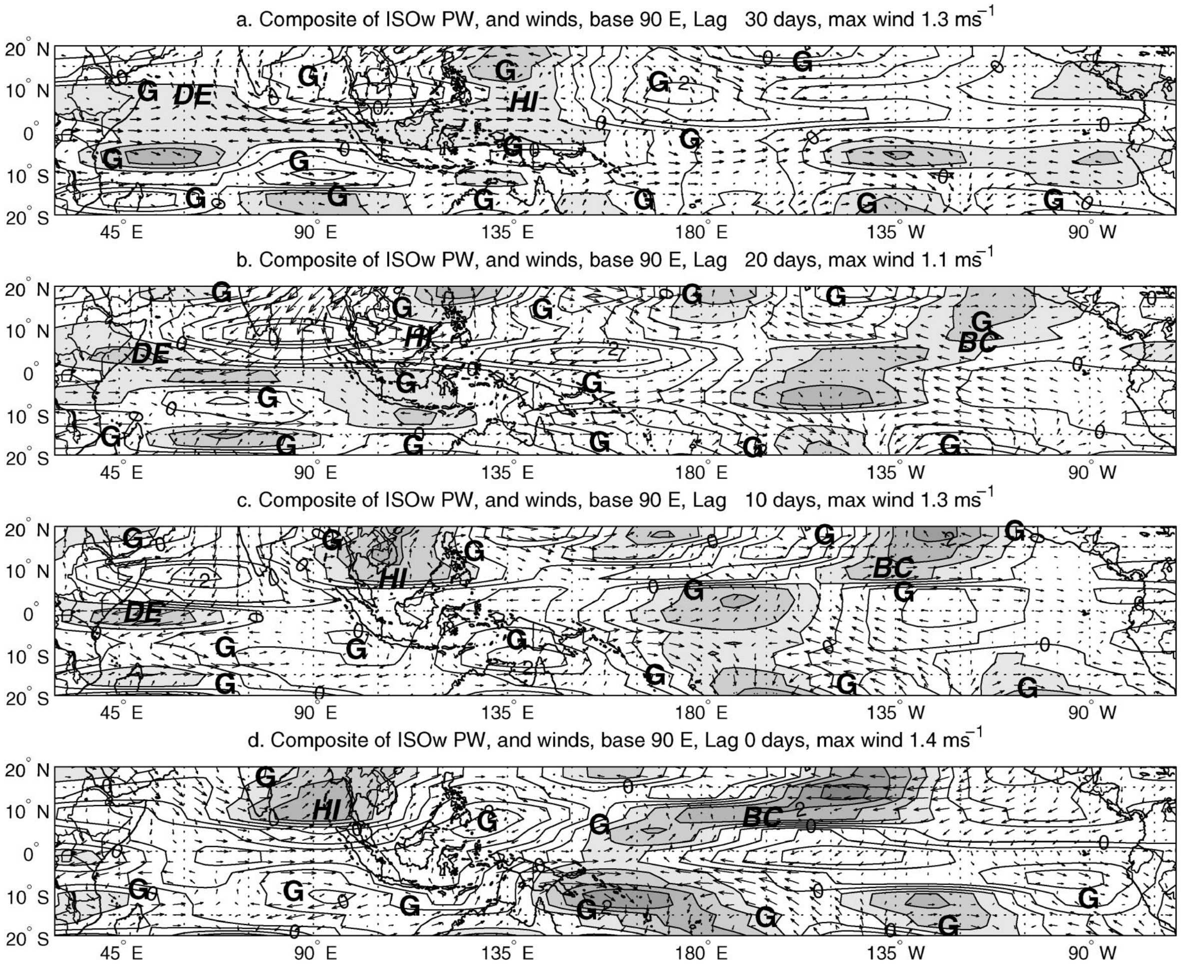
a. Composite of ISOw PW, and winds, base 90 E, Lag 30 days, max wind 1.3 ms^{-1}

b. Composite of ISOw PW, and winds, base 90 E, Lag 20 days, max wind 1.1 ms^{-1}

c. Composite of ISOw PW, and winds, base 90 E, Lag 10 days, max wind 1.3 ms^{-1}

d. Composite of ISOw PW, and winds, base 90 E, Lag 0 days, max wind 1.4 ms^{-1}

FIG. 2. Lagged regression composite of ISOw-filtered PW and 300-hPa NCEP–NCAR reanalysis winds, based on filtered OLR at 10°S, 90°E; positive PW anomalies are given dark shades: (a) lag = −30 days, (b) lag = −20 days, (c) lag = −10 days, (d) lag = 0 days, (e) lag = 10 days, (f) lag = 20 days, (g) lag = 30 days, (h) lag = 40 days. Approximate circulation centers are labeled with the letter G. Boldface and italic pairs of letters label anomalies responsible for trajectories in Fig. 1. Note that gyre labels are not in italic text.

except that the equatorial gyre is displaced somewhat southward and the Southern Hemisphere gyre is weaker and displaced eastward. The southward displacement of the gyre makes the basic structure similar to an $n = 1$ Rossby wave, with a saddle point in the winds located near (but slightly north of) the equator and 60°E.

The structure most similar to the $n = 1$ Rossby wave in Fig. 2 is shown in panel d centered west of the date line. This wave contains a pair of PW anomalies that are nearly symmetric across the equator and a saddle point in the winds centered just south of the equator. The second mode appears to dominate this composite, especially in the Eastern Hemisphere and at earlier lags. Antisymmetric PW anomalies (consistent with the second mode) occur throughout the composite (e.g., Fig. 2a, near 90°E). As discussed above, we repeated this regression analysis by using several different base points to examine the effect of the seasons on these interactions. Composites based along and just north of the equator were dominated by mode-1 Rossby waves instead of mode 2. These results indicate that the strong but highly asymmetric ISOe of the southern summer preferentially excites the second mode as it interacts with South America, whereas the nearly symmetric ISO of the northern spring preferentially excites the first mode [consistent with Kelvin wave reflection (McPhaden and Gill 1987)]. Structures seen at higher lags in Fig. 2 would tend to be dominated by events later in the active season, thus resulting in a stronger symmetric signal later in the composite.

c. *Composite ISOe plan view*

The composite of ISOe band-filtered data (Fig. 3) is similar to that of Hendon and Salby (1994) except that ours shows PW anomalies instead of OLR and reveals many more significant cycles as a consequence of our focus on the southern summer. Our composite is also less symmetric across the equator than theirs because ours is dominated by the southern summer during which

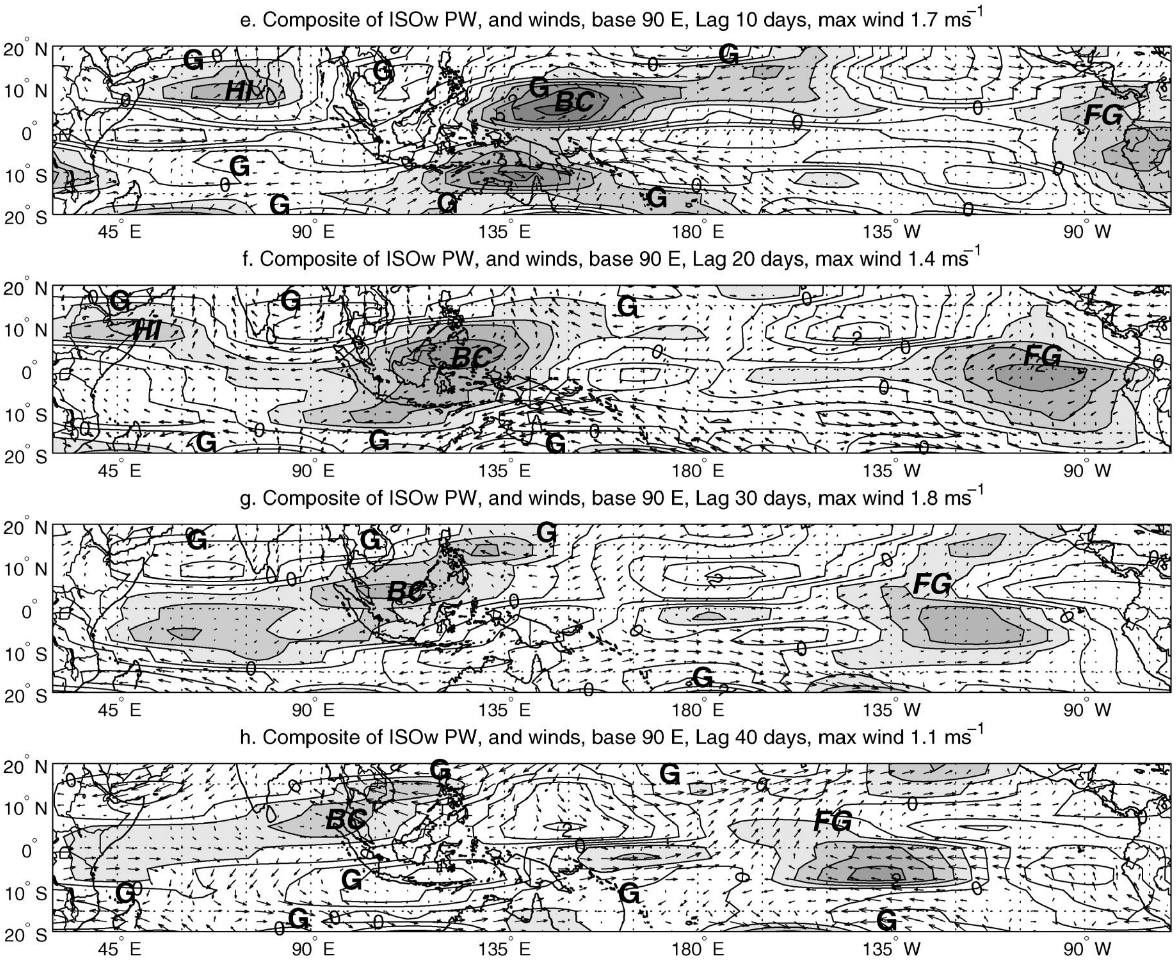

e. Composite of ISOw PW, and winds, base 90 E, Lag 10 days, max wind 1.7 ms^{-1}

f. Composite of ISOw PW, and winds, base 90 E, Lag 20 days, max wind 1.4 ms^{-1}

g. Composite of ISOw PW, and winds, base 90 E, Lag 30 days, max wind 1.8 ms^{-1}

h. Composite of ISOw PW, and winds, base 90 E, Lag 40 days, max wind 1.1 ms^{-1}

FIG. 2. (*Continued*)

Southern Hemisphere anomalies are stronger than Northern Hemisphere anomalies. The general wind patterns of the two sets of composites are similar.

Several significant events are visible in Fig. 3, and those along the equator can be compared with Fig. 1a. The equatorial portion of the PW anomaly in Figs. 3a–h (labeled *EF*) is traced by trajectory *EF* in Fig. 1c. Anomaly *EF* amplifies in Figs. 3a–c after the previously mentioned westward-propagating anomaly labeled *DE* (in Figs. 2a–d) arrived over the western Indian Ocean, and the equatorial portion of *EF* continues to at least the lag of 20 days as indicated in Fig. 3h. At lags of −30 to −20 days (Figs. 3a,b), the moist anomaly *EF* is in the 850-hPa easterly winds of the previous ISOe event. In Figs. 3c,d, *EF* migrates into a region of confluence. The disturbance associated with EF contains three PW anomalies that first become visible in Fig. 3b, one on the equator labeled *EF*, another weaker anomaly (labeled *EFN*) near 15°N, and another (labeled *EFS*) near 15°S. This trifurcation is likely related to the development and amplification of the convectively forced Rossby gyres (Hendon and Salby 1994). *EFS* and *EFN* lag behind *EF*. By lag = 20 days (Fig. 3f) *EF* begins to dissipate. *EFN* and *EFS* continue slowly eastward to near 150°W (near 15°N and 10°S) before they dissipate.

The upper-level winds (not shown) and the moisture anomalies appear to decouple where the upper-level wind anomaly begins to accelerate eastward and anomaly *EF* begins to dissipate. Convection and the upper-level winds decouple at about the same time that the low-level zonal wind disturbance begins to impinge on the Americas. The mountains may resist the ISOe-induced low-level flow and aid in decoupling the upper-level flow from convection and the lower-level flow. The base-state suppression of convection in the same region may aid in this decoupling process.

The pattern followed by the labeled anomalies in the ISOe composite is consistent with results of previous studies. The ISOe PW anomaly evolves through a process of growth over the Indian Ocean and decay over the western Pacific, reaching their highest amplitudes over the central Indian Ocean. The associated amplitudes there far exceed the amplitudes of related anomalies in the central and eastern Pacific and Atlantic ba-

a. Composite of ISOe PW, and winds, base 90 E, Lag −30 days, max wind 3 ms^{-1}

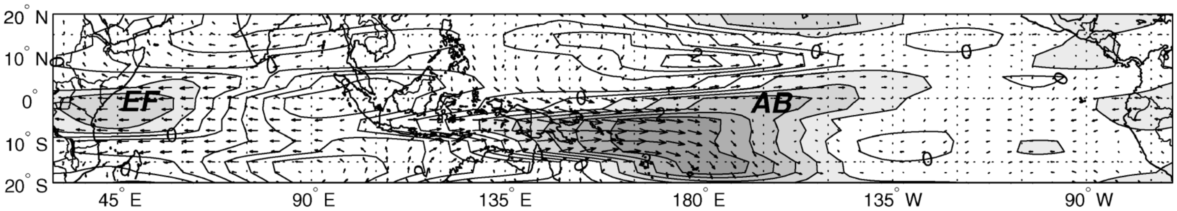

b. Composite of ISOe PW, and winds, base 90 E, Lag −20 days, max wind 3.3 ms^{-1}

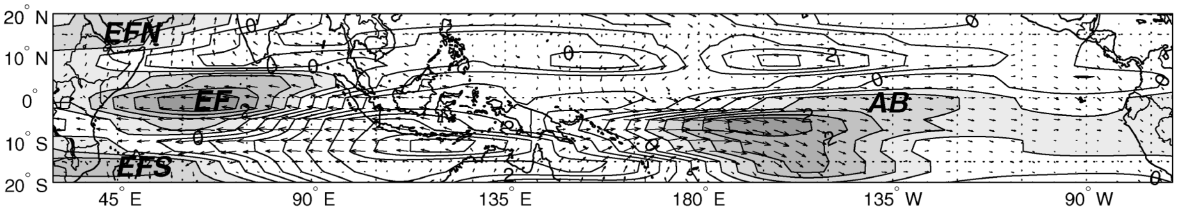

c. Composite of ISOe PW, and winds, base 90 E, Lag −10 days, max wind 4.1 ms^{-1}

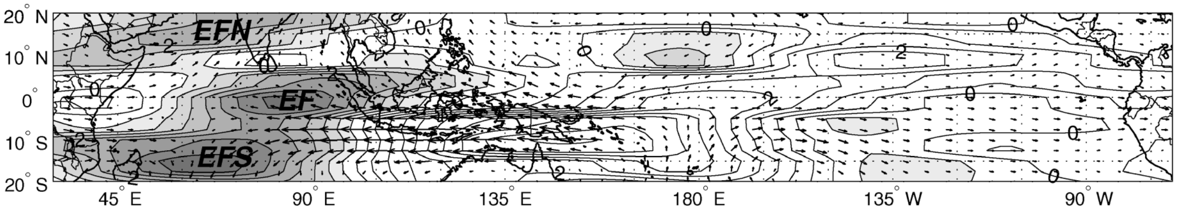

d. Composite of ISOe PW, and winds, base 90 E, Lag 0 days, max wind 4.6 ms^{-1}

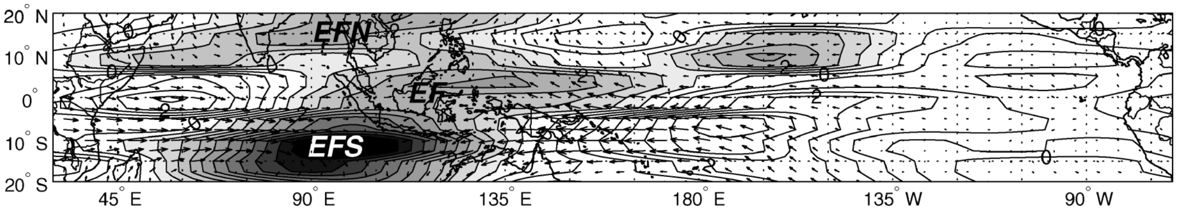

FIG. 3. As in Fig. 2 except for ISOe-filtered data.

sins, but that does not imply that ISOe-related disturbances do not play significant local roles in the latter two areas. Disturbances in the east Pacific and Atlantic basins are known to be related to the ISOe because they can usually be traced back to ISOe wind disturbances in the Indian Ocean (Kleeman 1989).

d. Composite sum (ISOe + ISOw)

The sum of ISOe and ISOw data gives the net variation of the composite. Quasi-standing activity in the composite is most easily discerned by plotting that sum, averaged over a latitude band, in a longitude–time diagram. Figure 4 shows the composite ISOe + ISOw PW for the equatorial region, averaged from 5°S to 5°N. Other latitude bands give results that vary from Fig. 4. For example, over the central Pacific, a band between 10° and 15°N often has anomalies with signs opposite those seen in the equatorial band. The ISOe is largely responsible for this behavior because it often consists of a PW anomaly at the equator bordered on the north and the south by anomalies with signs opposite that of the equatorial anomaly (e.g., anomaly *EF* near the date line in Fig. 3g). Figure 4 shows that eastward propagation is most evident in the Eastern Hemisphere, westward propagation is more evident in the Western Hemisphere, and quasi-standing behaviors are visible globally. Five vertical lines labeled A–E are included to guide the eye of the reader to most of the locations exhibiting quasi-standing oscillation patterns. Lines A and D are close to two main regions of high coherence shown in appendix A, which are located just east of the East African Highlands (A), and just west of the Andes Mountains (D). Line E is located over continental Africa, and may be caused by alternating anomalous zonal flow across the topography. Lines B and C are close to the other two bands of high coherence between 90°E and 90°W (appendix B). The regions of high coherence discussed in appendix B do not line up exactly with the standing activity seen in Fig. 4 because the coherence estimate includes the entire year so that it does not account for the seasonality of the process. It is clear from Fig. 4 and from appendix B that standing oscillation

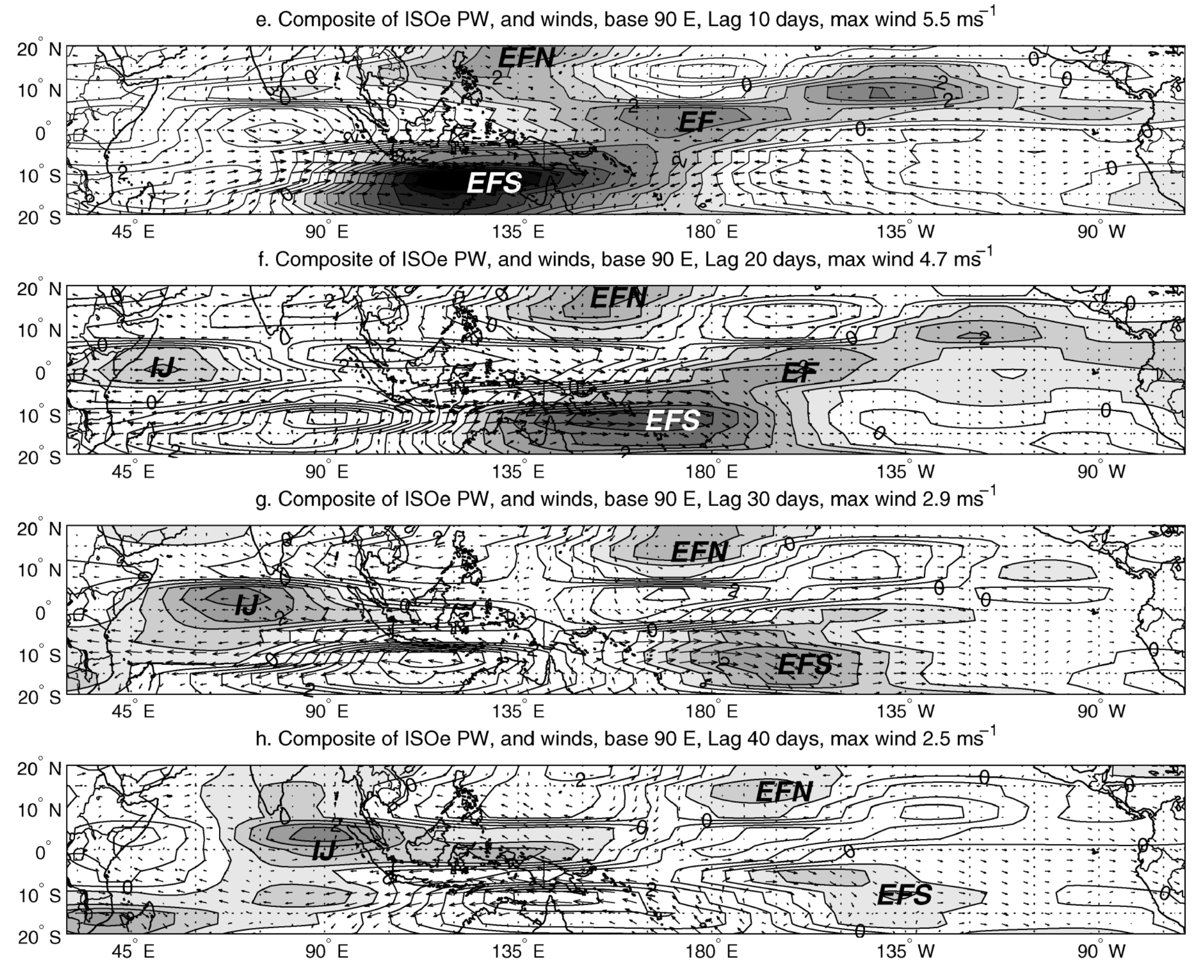
e. Composite of ISOe PW, and winds, base 90 E, Lag 10 days, max wind 5.5 ms^{-1}

f. Composite of ISOe PW, and winds, base 90 E, Lag 20 days, max wind 4.7 ms^{-1}

g. Composite of ISOe PW, and winds, base 90 E, Lag 30 days, max wind 2.9 ms^{-1}

h. Composite of ISOe PW, and winds, base 90 E, Lag 40 days, max wind 2.5 ms^{-1}

FIG. 3. (*Continued*)

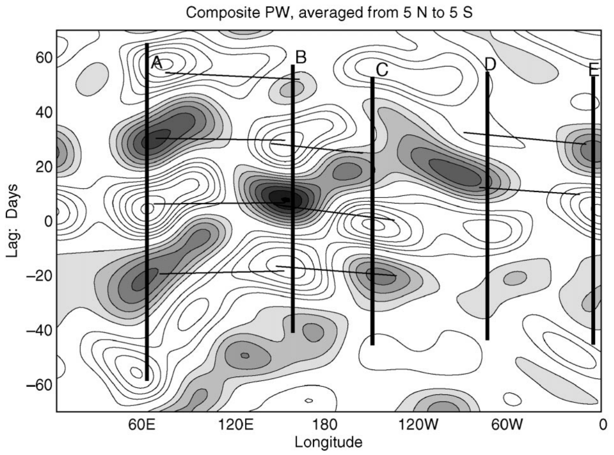
Composite PW, averaged from 5 N to 5 S

FIG. 4. Sum of the lon–time lag composite ISOe and ISOw PW, averaged from 5°N to 5°S. Vertical lines represent centers of quasi-standing behavior. The thin nearly horizontal lines represent seesaw-type standing events. The contour interval is 0.5 mm, and the zero line is omitted.

patterns comprise a major portion of the total intraseasonal variability.

Most of the standing behavior in Fig. 4 may be related to interactions between eastward and westward propagating waves. The forms of the eastward- and westward-propagating modes can often be distinguished in ISOe and ISOw band-filtered OLR data at locations and times that standing behavior occurs. Standing behavior often occurs in seesaw-type pairs between lines A and B (Lau and Chan 1986; Zhu and Wang 1993) and between lines C and D. Some such pairs are connected by thin nearly horizontal lines in Fig. 4. The composite standing behavior in the Eastern Hemisphere seems to result from interaction between eastward-propagating waves with velocities of around 5 m s^{-1} and dynamically different westward-propagating waves with phase speeds of between 3.5 and 4.5 m s^{-1}. Such behavior is possible because the apparent reflection points that relate the anomalies are fixed or approximately fixed in space. These results reveal that quasi-standing behavior at intraseasonal time scales is important in several regions around the globe. This type of interaction explains why total convection along the path of an MJO occasionally flares up. These flare-ups occur where the convectively enhanced regions of both eastward- and westward-moving modes intersect.

4. Discussion

The interactions between ISOe and ISOw modes and between waves and orographic features create quasi-standing variations at preferred locations that comprise a major portion of the net observed variations in the ISO frequency band (up to 50% of the local variability in some preferred regions, e.g., appendix B and Fig. 4). Filtering and regression techniques reveal that westward-propagating disturbances that are similar in certain regions to first meridional mode westward-propagating ER waves are important to the ISO process. These waves appear to be triggered primarily by interactions between the eastward-propagating portions of ISO disturbances with eastern basin barriers such as north–south mountain ranges and possibly by ISOe-modulated convection. Interactions between these westward-propagating waves and ISOe convection modulate the amplitudes of the westward-propagating waves. The moisture and convective anomalies of these waves tend to amplify when they propagate through regions of enhanced ISOe convective activity, giving the appearance that the waves form in those regions.

After reaching eastern Africa, these ER waves can, in turn, amplify existing ISOe disturbances or generate new ones through a process whose consequences are similar to those of partial reflection from the land barrier at the western boundary of the Indian Ocean basin. Quasi-standing oscillations in convection associated with the intersections of these waves generate flare-ups in total convection along the path of the ISOe.

The net ISO anomaly pattern (Fig. 4), together with the result of a local coherence test of ISOe and ISOw filtered PW data (appendix B), show that quasi-standing oscillations in convection and moisture are an important component of the total variability of these phenomena in many locations. Many of these quasi-standing oscillations appear to be consistent with interactions between the waves and the apparent reflections they produce.

Interactions between eastward- and westward-propagating modes are also responsible for other aspects of the behavior of the ISO and the westward-propagating waves, including the eastward pseudogroup velocity of the long ER waves. These interactions also help locate the main region of ISOe formation over the western Indian Ocean. The preferred wavenumbers and frequencies of both the ISOe and the ISOw disturbances may also be related to these wave–land/convective interactions. Eastward and westward propagating modes with specific phase speeds appear to have a tendency to resonate with each other at specific locations and at specific times to produce disturbances of the wavenumber and frequency ranges that we observe. The observed standing behavior occurs in specific regions because the land/convective interaction points are approximately fixed in space.

Interactions similar to those shown in our composite are observed throughout the seasonal cycle with varying statistics. Figure 5 shows some example observations of behaviors seen in the composites. Figure 5a shows unfiltered OLR anomalies (shaded) along with overlaid contours of the associated positive ISOe (red) and ISOw (blue) PW anomalies. One particularly strong westward-moving disturbance began around 19 February over the east Pacific when a positive ISOe PW anomaly traversed the Andes. This westward-moving anomaly is clearly visible in both the ISOw PW and in the unfiltered OLR anomalies. It traversed the Pacific and Indian Ocean basins and arrived at East Africa 19 April—at the same time that the ISOe PW indicates the arrival at the same location of an existing ISOe from the Western Hemisphere. These events were followed by the development of a new active ISOe, which subsequently crossed the Indian Ocean basin. The ISOw PW anomalies shown in Fig. 5a are consistent with OLR anomalies of the $n = 1$ ER band of WK99 (not shown). However, during different time periods (especially during the southern summer), the ISOw band is not dominated by the faster anomalies of the WK99 $n = 1$ ER band. For example, Fig. 5b shows the ISOw band PW for the period fall 1988 through early spring 1989, overlaid with contours of OLR anomalies filtered for the wavenumbers and frequencies $n = 1$ ER band of WK99 [filtering for cross-equatorial symmetry (WK99) was not included in this example]. OLR is shown here to be consistent with WK99. The anomalies seen in this example of the ISOw PW data are often slower than those seen in the corresponding ER band OLR. Though the ISOw disturbances shown in panel a are structurally similar to the corresponding $n = 1$ ER band OLR anomalies, those shown in the period in panel b are not well described by the $n = 1$ ER band alone. Most ER $n = 1$ band anomalies shown in panel b are not independent disturbances. Instead, they are contributing to the shapes of lower-frequency, more slowly propagating anomalies. The slow mode shown in ISOw PW data in panel b is similar to the slow mode seen in our composites. The composite waves shown in Fig. 1 and those seen in Fig. 5b appear to be dominated by the second meridional mode, whereas those appearing in Fig. 5a and in our composite that is based at the equator (not shown) appear to be dominated by the first mode.

These observed interactions play fundamental roles in the Intraseasonal oscillations. Our ongoing research indicates that these interactions may be used to improve statistical models for enhanced long-term prediction of ISOs.

Acknowledgments. This work was funded by a grant from the National Science Foundation, ATM 0003351, and by a supplemental fellowship from the NASA Penn-

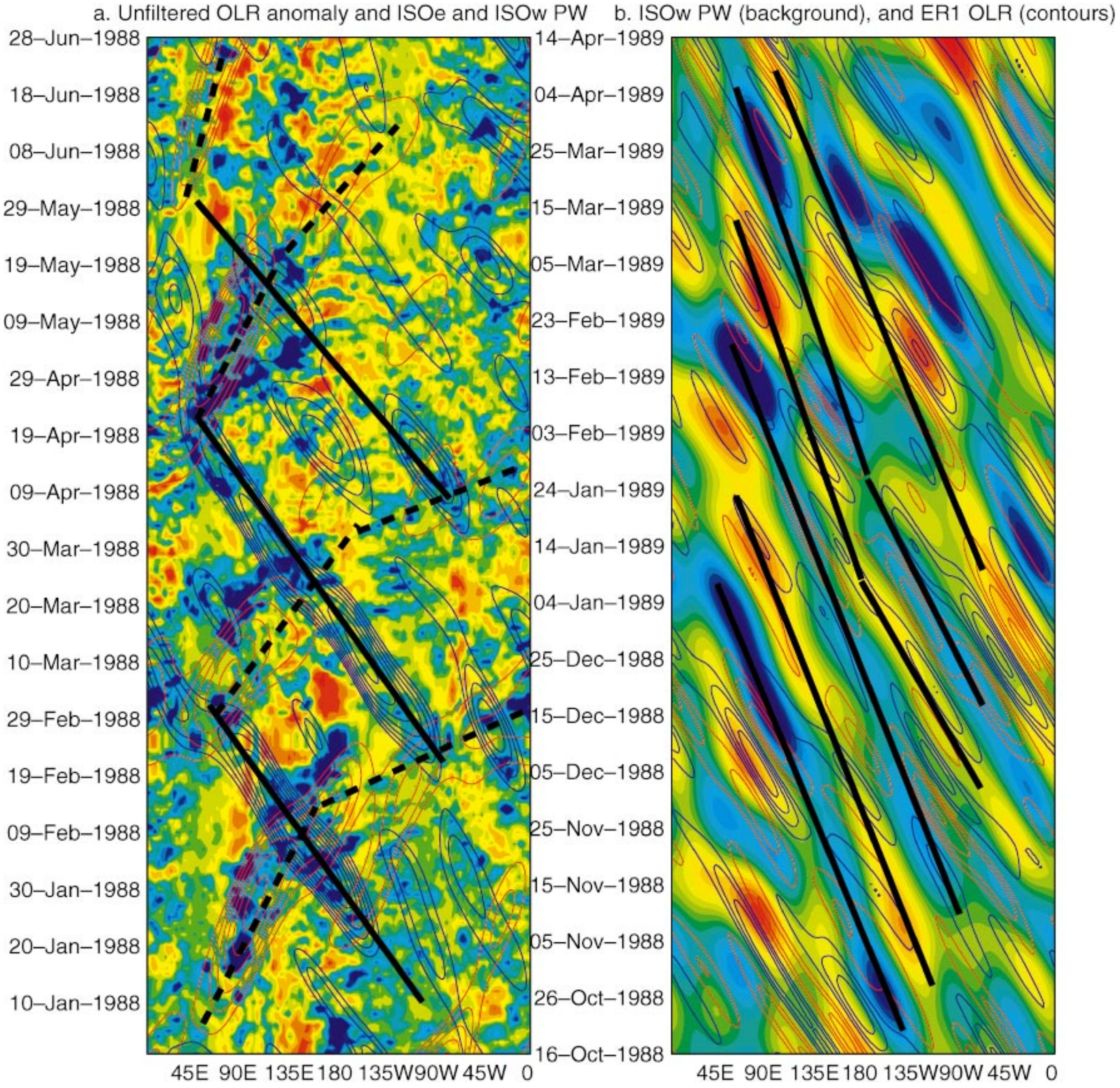

FIG. 5. Example cases of behaviors similar to those seen in the composite. (a) Pattern of related interactions seen during the period northern winter through spring, 1988. Unfiltered OLR anomalies are shown shaded in the background. The range of the shading is −80 to +80 W m^{-2}. Positive ISOw PW anomalies are indicated by blue contours. Positive ISOe PW anomalies are indicated by red contours. Solid black lines approximate trajectories of ISOw PW anomalies. Dashed lines approximate trajectories of ISOe PW anomalies. (b) Comparison of ISOw PW anomalies (shaded in the background) and contours of ER1 band-filtered OLR (see WK99, except we did not apply symmetry filtering). Solid lines approximate trajectories of some examples of slow-moving ISOw anomalies. The background shading range is from −7 (blue) to +7 (red) mm PW.

sylvania Space Grant Consortium. Dr. George Kiladis graciously provided comments and an additional review.

APPENDIX A

Statistical Significance Testing

a. Testing method

The bootstrap (Wilks 1995) is a nonparametric resampling test, meaning that it does not require an analytical approximation for the sampling distribution. Randomly resampling the data and calculating results again for each new sample determines the distribution of results used to apply the test. To resample the data we gave each day in a gridpoint time series an index number, then randomly selected the components of a vector **r** from the set of indices. Values in the original time series corresponding to the set of indices in **r** were assigned to the new resampled series in the same order that the indices appear in **r**. The resampled series were the same length as the series used to calculate the reported regression model results. The resampling method

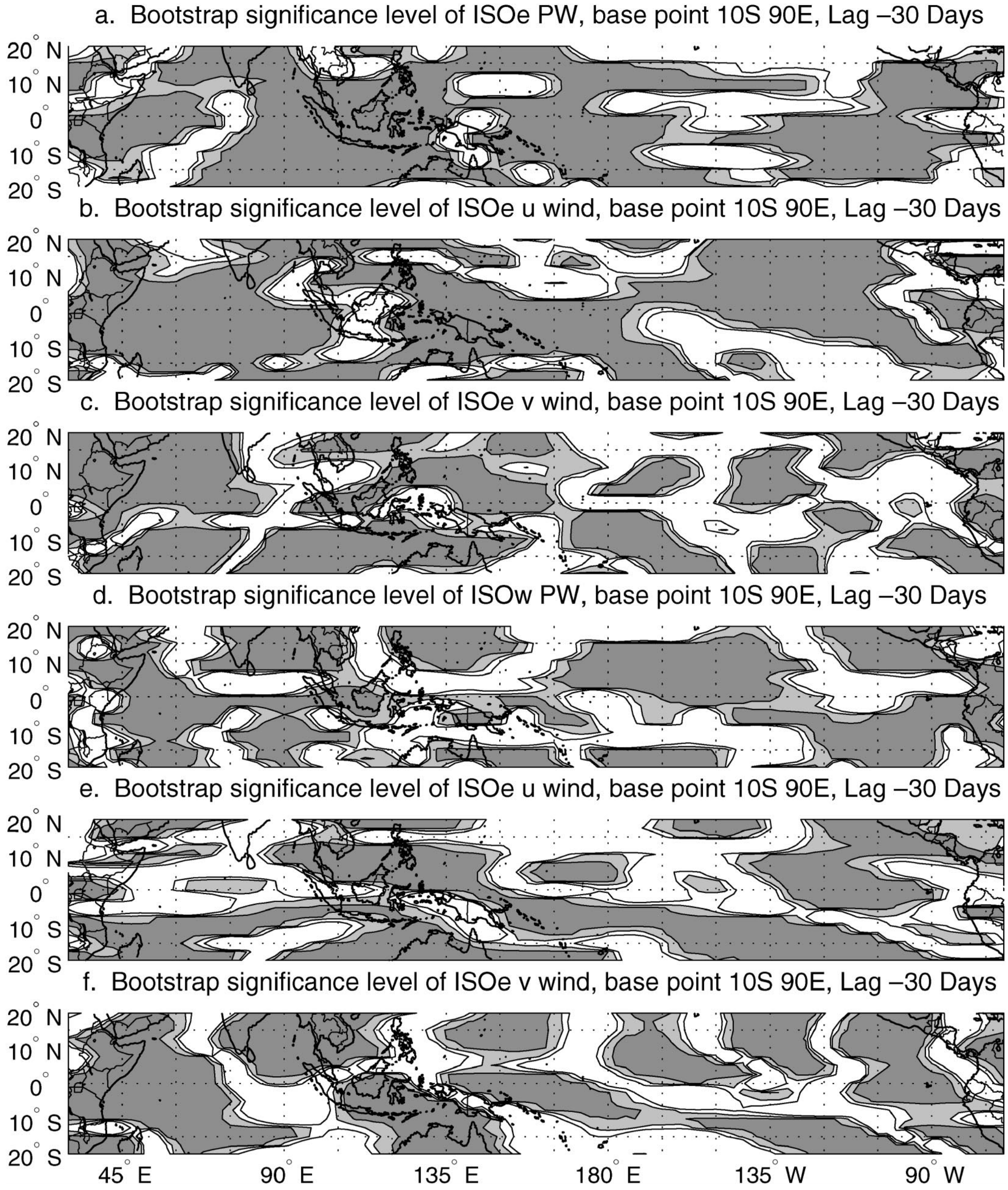

FIG. A1. Maps of bootstrap statistical significance estimates for the ISOe regression composite results, given for lag = −30 days (cf. Figs. 2 and 3a). The 90%, 95%, and 99% levels are contoured. The region between the 90% and 95% levels is not shaded. The regions between the 95% and 99% levels are shaded light gray, and the regions exceeding the 99% level dark gray. (a)–(c) ISOe-filtered data and (d)–(f) ISOw-filtered data; (a) and (d) are the precipitable water results; (b) and (e) the *u* wind results; and (c) and (f) the *v* wind results.

allowed that a specific index might never be included in **r**, or it could be included once or multiple times. Time lags were preserved in the regression models by resampling y with the vector **r** and by resampling x_1 with the vector $\mathbf{r} - \tau$. The series for the higher-power terms were then calculated from the resulting lagged x_1. We included 400 resampling calculations in each distribution and assumed the null hypothesis that the model disturbance was not significantly different from zero. The position of the zero anomaly in the distribution determined statistical significance. If 90% of the realizations were above or below the zero anomaly line, then the disturbance was considered to achieve the 90% significance level.

b. Significance test results

Figure A1 shows the bootstrap statistical significance results for each variable in Figs. 2b and 3b. All statistical significance results cannot be included here because of space considerations, but the given results are representative of the behavior of the others. Shading levels represent the 95% and 99% levels. The darkest shading represents regions exceeding the 99% level, and the curve enclosing the regions exceeding the 95% level is labeled.

With few exceptions, regions with insignificant anomalies are those regions where the magnitudes of the anomalies are close to zero. Exceptions are immediately adjacent to the coast of East Africa in the ISOe *u* wind result, and in the central Pacific and western Maritime Continent region in the ISOe PW result. The ISOe PW result appears to be insignificant north and south of the climatological intertropical convergence zone in the central Pacific basin. The variable exhibiting the least significance globally is the ISOe *v* wind. The ISOe *v* wind exhibits smaller anomalies than the dominant ISOe *u* wind, consistent with this significance result.

One of the most important results of this significance test is that the westward-propagating disturbances associated with the ISOe in the ISOw result (Fig. 2) are significantly different from zero and are thus likely to be important to ISOe dynamics because of the relationships observed in the composite model. Significance results are similar for other time lags, except that the low significance regions where anomalies are small move as the anomalies evolve.

APPENDIX B

Squared Coherence Tests

a. Coherence tests

Squared coherence was used here to find the most probable locations and importance at those locations of standing behavior in the equatorial regions generated by interaction of anomalies in ISOe- and ISOw-filtered data (e.g., Hayashi 1979). If there exists some relationship between ISOe- and ISOw-filtered data that results in standing behavior, both datasets should have high squared coherence at the locations where the standing behavior often occurs. We tested his concept by averaging the filtered data over the 5°S to 5°N band and finding the squared coherence of the resulting ISOe and ISOw PW data at each longitude grid point. The squared coherence was calculated as discussed below.

b. Methodology

The squared coherence C_{xy} was calculated as in Eq. (B1) (below) by using Welch's method of power spectrum estimation (Rabiner and Gold 1975; Welch 1967) and by following Hayashi (1982). Let x represent the time series of ISOw band-filtered PW at a given longitude and y represent the time series of ISOe band-filtered OLR at the same longitude:

$$C_{xy} = \frac{\mathrm{abs}(P_{xy})^2}{P_{xx}P_{yy}}, \tag{B1}$$

where P_{xy} is the cross-spectral density found by averaging the products of the discrete Fourier transforms of the segments of the x and y time series and where P_{xx} and P_{yy} are the power spectral densities of x and y, respectively. Time series were analyzed by separating them into many consecutively overlapping 100-day segments. These segments were modified by multiplying them by cosine bells (a Hanning window) and by padding them with zeroes to a length of 256 days (to allow use of the fast Fourier transform). The overlap between segments was 60 days. This overlap functions to recover data that was lost because of the tapering. Statistical significance was assessed by assuming the null hypothesis that the pairs of time series are random and unrelated. One thousand pairs of series of random numbers were developed and analyzed as above. The null hypothesis was rejected at the 99% significance level (the value beyond which only nine results of the squared coherence between the random datasets fell, or about 0.07). The phase of the coherent relationship was also calculated. This was done in part by following Eq. (B2):

$$\mathrm{phase} = \tan^{-1}\left[\frac{\mathrm{Im}(P_{xy})}{\mathrm{Re}(P_{xy})}\right], \tag{B2}$$

where Im and Re designate the imaginary and real parts. Note that this analysis is applied to the entire dataset, as stated, without regard to seasonality. The standing behavior visible in Fig. 4 is diagnosed in a manner that emphasized the southern summer. Hence, the coherence and composite results are not expected to agree exactly.

c. Results

Figure B1 gives the estimates of local coherence between 5°N–5°S mean ISOe and ISOw bandpass-filtered PW. Local squared coherence never exceeds about 0.30 (corresponding with a coherence of about 55%), though it is significant at many locations and frequencies. The phase of the local coherent relationship is plotted in the vectors superimposed on the diagram.

Figure B1 shows that two main regions of high coherence occur in the 30–60-day band. One of these occurs near 50°E along the east coast of Africa. The other occurs near 90°W off the west coast of South America. The phase relationships shown for these two regions are opposite. These results indicate that standing behavior may account for as much as half of the variability in the ISOe- and ISOw-filtered data in this latitude band at locations east of Africa and west of South America. Two other bands of significant coherence occur at mainly lower frequencies between 90°E and 90°W. The regression model provides information about the structure and propagation of the ISOw modes that are linearly

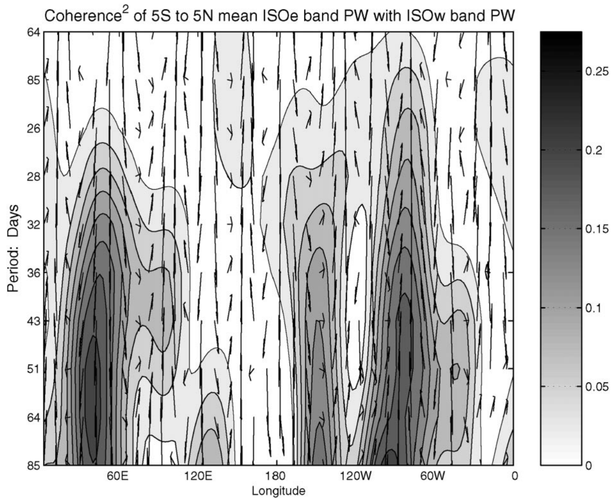

FIG. B1. Local coherence of ISOe band with ISOw band PW in the equatorial region, calculated across the annual cycle. Reveals where standing behavior likely occurs. Phase vectors are plotted over the diagram. Vectors pointing to the right indicate zero phase, and phase increases counterclockwise.

and nonlinearly coherent with the ISOe (Figs. 2–3). A composite similar to Fig. 4 but with the base point at the equator (not shown) agrees better with this coherence analysis than does the standing behavior in Fig. 4.

REFERENCES

Anderson, J. R., and D. E. Stevens, 1987: The response of the tropical atmosphere to low frequency thermal forcing. *J. Atmos. Sci.,* **44,** 676–686.

Battisti, D. S., 1988: Dynamics and thermodynamics of a warming event in a coupled tropical atmosphere–ocean model. *J. Atmos. Sci.,* **45,** 2889–2929.

Chang, C.-P., 1977: Viscous internal gravity waves and low-frequency oscillations in the tropics. *J. Atmos. Sci.,* **34,** 901–910.

Draper, N. R., and H. Smith, 1966: *Applied Regression Analysis.* John Wiley & Sons, 407 pp.

Hayashi, Y., 1979: A generalized method of resolving transient disturbances into standing and traveling waves by space–time spectral analysis. *J. Atmos. Sci.,* **36,** 1017–1029.

——, 1982: Space–time spectral analysis and its application to atmospheric waves. *J. Meteor. Soc. Japan,* **60,** 156–171.

——, and S. Miyahara, 1987: A three-dimensional linear response model of the tropical intraseasonal oscillation. *J. Meteor. Soc. Japan,* **65,** 843–852.

Hendon, H. H., and M. L. Salby, 1994: The life cycle of the Madden–Julian oscillation. *J. Atmos. Sci.,* **51,** 2225–2237.

Hu, Q., and D. A. Randall, 1994: Low-frequency oscillations in radiative–convective systems. *J. Atmos. Sci.,* **51,** 1089–1099.

Itoh, H., and N. Nishi, 1990: Considerations for the structure of the tropical intraseasonal oscillation. *J. Meteor. Soc. Japan,* **68,** 659–675.

Kang, I. S., and S. I. An, 1998: Kelvin and Rossby wave contributions to the SST oscillation of ENSO. *J. Climate,* **11,** 2461–2469.

Kemball-Cook, S., and B. Wang, 2001: Equatorial waves and air–sea interaction in the boreal summer intraseasonal oscillation. *J. Climate,* **14,** 2923–2942.

Kiladis, G. N., and M. Wheeler, 1995: Horizontal and vertical structure of observed tropospheric equatorial Rossby waves. *J. Geophys. Res.,* **100** (D11), 22 981–22 997.

Kleeman, R., 1989: A modeling study of the effect of the Andes on the summertime circulation of tropical South America. *J. Atmos. Sci.,* **46,** 3344–3362.

Lau, K., and P. H. Chan, 1986: Aspects of the 40–50 day oscillation during the northern summer as inferred from outgoing longwave radiation. *Mon. Wea. Rev.,* **114,** 1354–1367.

Liebmann, B., and C. A. Smith, 1996: Description of a complete (interpolated) outgoing longwave radiation dataset. *Bull. Amer. Meteor. Soc.,* **77,** 1275–1277.

Lin, J. W.-B., J. D. Neelin, and N. Zeng, 2000: Maintenance of tropical intraseasonal variability: Impact of evaporation–wind feedback and midlatitude storms. *J. Atmos. Sci.,* **57,** 2793–2823.

Lindzen, R. S., 1974: Wave-CISK in the tropics. *J. Atmos. Sci.,* **31,** 156–179.

Madden, R. A., and P. R. Julian, 1994: Observations of the 40–50 day tropical oscillation—A review. *Mon. Wea. Rev.,* **122,** 814–837.

Matsuno, T., 1966: Quasi-geostrophic motions in the equatorial area. *J. Meteor. Soc. Japan,* **44,** 25–43.

McPhaden, M. J., and A. E. Gill, 1987: Topographic scattering of equatorial Kelvin waves. *J. Phys. Oceanogr.,* **17,** 82–96.

Park, C. K., and S. D. Schubert, 1993: Remotely forced intraseasonal oscillations over the tropical Atlantic. *J. Atmos. Sci.,* **50,** 89–103.

Rabiner, L. R., and B. Gold, 1975: *Theory and Application of Digital Signal Processing.* Prentice-Hall, 762 pp.

Randel, D. L., T. H. Vonder Haar, M. A. Ringerud, G. L. Stephens, T. J. Greenwald, and C. L. Combs, 1996: A new global water vapor dataset. *Bull. Amer. Meteor. Soc.,* **77,** 1233–1246.

Roundy, P. E., and W. M. Frank, 2004a: A climatology of waves in the equatorial region. *J. Atmos. Sci.,* **61,** 2105–2132.

——, and ——, 2004b: Applications of a multiple linear regression model to the analysis of relationships between eastward and westward moving intraseasonal modes. *J. Atmos. Sci.,* **61,** 3041–3048.

Salby, M. L., R. R. Garcia, and H. H. Hendon, 1994: Planetary-scale circulations in the presence of climatological and wave-induced heating. *J. Atmos. Sci.,* **51,** 2344–2367.

Straub, K. H., and G. N. Kiladis, 2002: Observations of a convectively coupled Kelvin wave in the eastern Pacific ITCZ. *J. Atmos. Sci.,* **59,** 30–53.

von Storch, H., and F. W. Zwiers, 1999: *Statistical Analysis in Climate Research.* Cambridge University Press, 494 pp.

Wang, B., 1988: Dynamics of tropical low-frequency waves: An analysis of the moist Kelvin wave. *J. Atmos. Sci.,* **45,** 2051–2065.

——, and X. Xie, 1997: A model for the boreal summer intraseasonal oscillation. *J. Atmos. Sci.,* **54,** 72–86.

Welch, P. D., 1967: The use of fast Fourier transform for the estimation of power spectra: A method based on time averaging over short, modified periodograms. *IEEE Trans. Audio Electroacoust.,* **AU-15,** 70–73.

Wheeler, M., and G. N. Kiladis, 1999: Convectively coupled equatorial waves: Analysis of clouds and temperature in the wavenumber-frequency domain. *J. Atmos. Sci.,* **56,** 374–399.

——, ——, and P. J. Webster, 2000: Large-scale dynamical fields associated with convectively coupled equatorial waves. *J. Atmos. Sci.,* **57,** 613–640.

Wilks, D. S., 1995: *Statistical Methods in the Atmospheric Sciences: An Introduction.* International Geophysical Series, Vol. 59, Academic Press, 467 pp.

Yamagata, T., and Y. Hayashi, 1984: A simple diagnostic model for the 30–50 day oscillation in the tropics. *J. Meteor. Soc. Japan,* **62,** 709–717.

Yanai, M., B. Chen, and W. Tung, 2000: The Madden–Julian oscillation observed during the TOGA COARE IOP: Global view. *J. Atmos. Sci.,* **57,** 2374–2396.

Zhang, C., and H. H. Hendon, 1997: Propagating and standing components of the intraseasonal oscillation in tropical convection. *J. Atmos. Sci.,* **54,** 741–752.

Zhu, B., and B. Wang, 1993: The 30–60 day convection seesaw between the tropical Indian and western Pacific Oceans. *J. Atmos. Sci.,* **50,** 184–199.